Megathrust Earthquakes Amplify Coastal Wave Hazards in Cascadia Under Rising Sea Levels

Cesar G. Lopez[1*] and Claire C. Masteller[1]

[1]Department of Earth, Environmental, and Planetary Sciences, Washington University in St. Louis, St. Louis, Missouri 63130, USA

*Corresponding author: c.g.lopez@wustl.edu

Abstract

Along the Cascadia Subduction Zone, destructive megathrust earthquakes represent a significant coastal hazard. These events generate abrupt, meter-scale coseismic subsidence, instantaneously increasing relative sea level, inundation extent, and the reach of ocean waves. In the coming decades, eustatic sea level rise will continue to shift baseline coastal conditions, with the potential to change earthquake-driven coastal hazards. Here, we model how sea level rise, wave climate, and the magnitude and timing of coseismic subsidence interact to influence nearshore wave dynamics at 32 rocky coast sites spanning diverse morphologies along the Cascadia margin. We find that coseismic subsidence amplifies shoreline wave power by shifting wave action landward and reducing energy dissipation, despite an overall reduction in wave breaking. This amplification is strongly controlled by shore platform slope, with negligible increases along steep rocky coasts and multiple orders-of-magnitude increases for low-gradient platforms. These changes highlight the potential for increases in wave-driven coastal erosion and shoreline retreat following future earthquakes. The timing and persistence of these earthquake-driven hazards depend strongly on the sea level rise trajectory. Under a high-emissions scenario, accelerated sea level rise shifts the window of maximum earthquake-driven amplification toward the beginning of the century, increasing the potential of post-event recovery. Our results demonstrate that interactions between sea level rise and episodic coseismic subsidence create transient, but potentially long-lived, shifts in coastal wave energy regimes that can shape future coastal hazards and landscape evolution. This coupling between climate and solid-Earth processes reveals a previously unrecognized control on coastal change along tectonically active margins.

Introduction

The Cascadia Subduction Zone (CSZ) stretches along the Pacific Northwest coast of North America, extending from the Mendocino Triple Junction in northern California to Vancouver Island in British Columbia (1). Formed through the subduction of the Gorda, Juan de Fuca, and Explorer plates beneath North America (2–4), the CSZ can generate some of the world's most powerful earthquakes (5, 6), with profound consequences for communities, infrastructure, and natural hazards along the coastline (7–9).

Paleoseismic records from the Cascadia Margin indicate earthquake recurrence intervals of 200 to 800 years, with an average of ~500 years for the largest events (10, 11), with the last large Cascadia earthquake occurring over 320 years ago in 1700 AD (12, 13). Time-dependent earthquake recurrence models indicate a 30% chance of a > M8 earthquake occurring in southern Cascadia in the next 50 years and a 10% to 15% chance of an approximately M9 rupture of the full subduction zone (14, 15). These recurrence estimates indicate that a future Cascadia megathrust earthquake is a realistic possibility within the coming century, motivating efforts to understand future coastal hazards driven by such a large-scale seismic event.

While megathrust earthquakes generate a range of immediate hazards, including strong ground shaking and tsunamis, they can also produce long lasting changes to coastal landscapes through coseismic vertical land motion. Coastal wetland stratigraphy (16–21) and geodetic modeling approaches (22–25) indicate that past Cascadia earthquakes can generate 0.5 to 2 m of instantaneous subsidence along portions of the coastline. This subsidence produces an abrupt increase in relative sea level, or relative sea level rise, that increases nearshore water depths, continuing to influence coastal processes and hazards long after the earthquake itself.

Relative sea level rise (RSLR) integrates eustatic sea level changes, gravitational effects, and local vertical land motion (26). In Cascadia, RSLR is driven both by climate-driven, eustatic sea level rise (SLR) and active tectonics, including both gradual interseismic uplift and punctuated coseismic subsidence during large earthquakes. Specifically, while interseismic uplift gradually elevates the coastline reducing RSLR, coseismic subsidence can produce instantaneous increases in RSLR (27), substantially amplifying coastal inundation and flooding hazards (8). At the same time, global sea levels are rising in response to climate change (28–30), increasing water levels along the entire Cascadia coastline. Although interseismic uplift has historically buffered the effects of eustatic SLR in portions of Cascadia (31), projected rates of global sea level rise are expected to outpace this tectonic buffering over the coming century (32, 33).

By 2100, global sea levels are projected to rise by 0.56 m (0.43 to 0.76 m) relative to baseline conditions from 1995 to 2014 under SSP2-4.5, a moderate emissions scenario. Under SSP5-8.5, a very high emissions scenario representing the upper envelope of emissions futures, sea level is projected to increase by 0.77 m (0.63 to 1.01 m). These projections are comparable to the lower bound of coseismic subsidence expected during a future Cascadia megathrust earthquake. Both the emissions trajectory and the timing of the next earthquake will determine the sea level baseline upon which meter-scale coseismic subsidence is superimposed. As such, future coastal hazards in Cascadia will be shaped by the interaction of climate-driven sea level rise and solid Earth processes that drive vertical land motion across the seismic cycle.

By altering nearshore water depths, RSLR controls the location of wave breaking and how efficiently offshore wave energy is transmitted to the coastline. Wave power (kW/m) is a key driver of coastal erosion, particularly on rocky coastlines with steep sea cliff topography (34, 35). Indeed, recent work across the U.S. West Coast demonstrated that tectonically-driven vertical land motion exerts a first order control on rocky shoreline retreat by modifying cliff-front wave power (36). Specifically, interseismic uplift can buffer shoreline retreat by shifting the locus of wave attack seaward, enhancing nearshore wave energy dissipation and reducing cliff-incident wave power. In contrast, subsidence increases nearshore water depths and shifts wave breaking landward, leading to enhanced cliff front wave power and more rapid coastal retreat.

Paired with rising sea levels, climate change is intensifying offshore wave climate, increasing the energy available for erosion as waves traverse the nearshore (37–40). How these compounding shifts in marine drivers will influence rocky coast erosion remains poorly constrained. Some studies suggest that increasing water depth at the base of coastal sea cliffs will propagate wave action landward, increasing cliff-front wave power and coastal erosion (41–43). Others have instead argued for the opposite effect, proposing that relatively deep water at the cliff base may drive hydrodynamic transitions that suppress nearshore wave breaking, thereby reducing wave power and erosion, with responses highly dependent on local shore platform morphology (44, 45).

Set against this shifting background of level rise and wave climate intensification, the response of Cascadia coastlines to a future megathrust earthquake remains highly uncertain. A recent compilation of shoreline retreat and uplift rates shows that even gradual subsidence enhances shoreline retreat relative to uplifting coastlines, likely by shifting wave action landward and increasing cliff-incident wave power (36). Whether this effect persists under the abrupt, meter-scale subsidence expected during CSZ earthquakes is unclear, as the same mechanisms that focus wave action under moderate sea level rise may instead suppress nearshore wave breaking if water depths increase substantially, effectively drowning the shore platform. This transition likely depends on nearshore bathymetry and pre-earthquake water levels, which set local wave breaking conditions. Depending on these factors, identical coseismic subsidence may either amplify or reduce cliff-incident wave power. The timing of a future Cascadia earthquake relative to the ongoing trajectory of sea level rise will itself modulate the coastal response, as background increases in nearshore water depth will progressively change wave breaking conditions independent of any coseismic perturbation. Given this, how coseismic subsidence and the compounding effects of SLR will combine to affect nearshore wave dynamics and future rocky coast erosion remains unresolved.

In this contribution, we model earthquake-driven changes in nearshore wave dynamics at 32 sites across Cascadia (Fig. 1) in response to the combined effects of coseismic subsidence and eustatic sea level rise. Selected sites have a diverse range of shore platform morphologies and cliff-base water levels, with many located within or near major population centers and recreational destinations. Across these sites, we explore a parameter space defined by earthquake timing, coseismic subsidence magnitude, century-scale trajectories of offshore wave climate (46) and sea level rise. Model simulations are run in hourly time steps from 2020 to 2100 under two emissions scenarios: SSP2-4.5 and SSP5-8.5. We systematically vary both earthquake timing (at decadal intervals) and coseismic subsidence magnitude (0.5, 1.0, and 2.0 m), using site-specific near-shore bathymetry as well as projected tidal levels and interseismic vertical land motion over the model period (Materials and Methods).

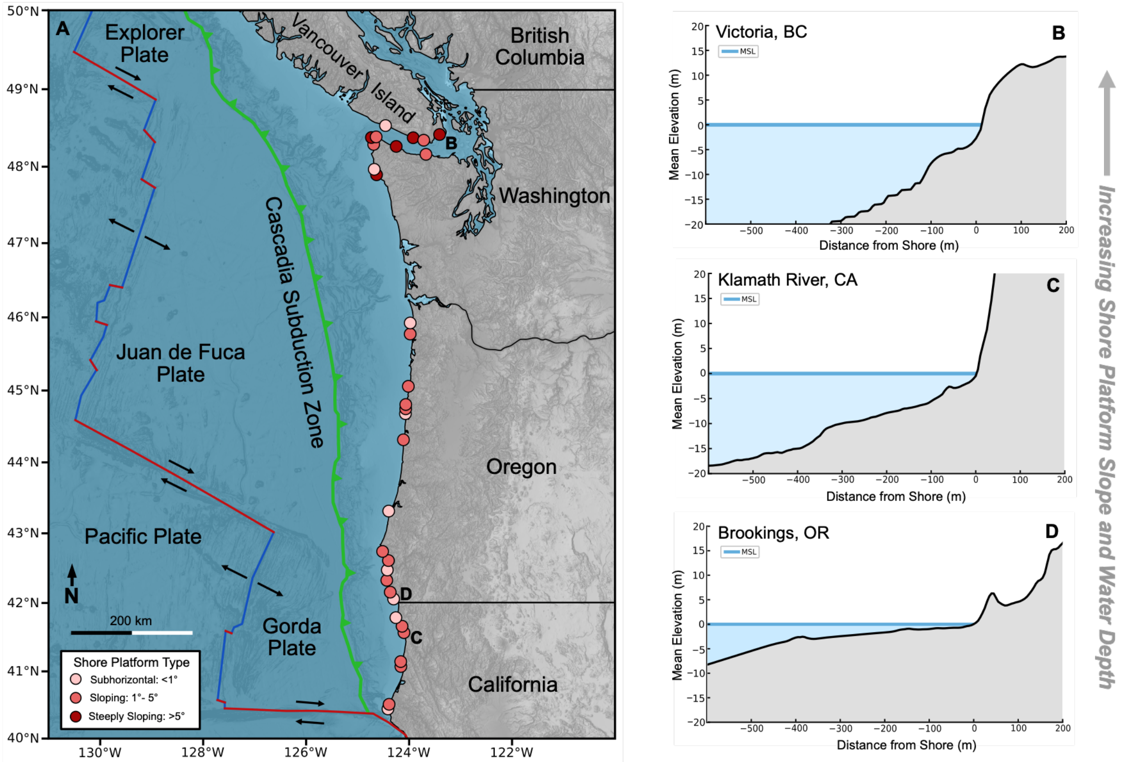

Figure 1. A) Map of Cascadia. Arrows denote tectonic plate motion direction and points represent the 32 study sites, which are colored based on the underlying shore platform slope class (47, 48). B-D.) Swath profiles for three study sites representing the three primary platform categories in order of descending slope. Site locations are denoted on the map by their respective letter.

Results

Earthquake-driven Changes in Nearshore Wave Transformations

To characterize the effects of coseismic subsidence and RSLR on nearshore wave dynamics, we first classify cliff-incident wave types as breaking, broken, and unbroken (Materials and Methods; 45). Breaking and broken waves dissipate energy at the coastline and can therefore drive erosion, whereas unbroken waves largely reflect from the cliff with minimal energy transfer or erosional contribution (62). Even in baseline scenarios without coseismic subsidence, climate-driven RSLR progressively suppresses nearshore wave breaking. By 2100, the number of breaking and broken waves declines by 8.5% to 19.8% under SSP2-4.5 relative to 2020 conditions. Under the high-emissions SSP5-8.5 scenario, this reduction increases to 8.5% to 26.7% across all sites.

Superimposed on this background trajectory, coseismic subsidence produces an instantaneous reduction in breaking and broken waves relative to non-earthquake conditions in the same year, with the magnitude of this reduction increasing strongly with subsidence (Fig. 2). Across all sites, earthquake timings, and emissions scenarios, median reductions in wave breaking range from 0.1% for 0.5 m of subsidence, to 1.1% for 1.0 m, and 9.2% for 2.0 m, with maximum reductions of 14.9%, 29.2%, and 53.4%, respectively (Fig. 2A, E). It is worth emphasizing that the median instantaneous reduction produced by 2.0 m of subsidence is comparable in magnitude to the reduction accumulated over the century through RSLR alone. Thus, a single earthquake can abruptly modify nearshore wave transformations by an amount comparable to decades of gradual climate-driven change. This response strengthens for earthquakes later in the century, particularly under SSP5-8.5, where the median reduction associated with 2.0 m of subsidence increases from 7.5% for an earthquake in 2030 to 24.0% in 2100, compared with an increase from 7.1% to 14.2% under SSP2-4.5. By 2100, the maximum wave breaking reductions reach 52.0% under SSP2-4.5 and 53.4% under SSP5-8.5, approximately twice the maximum centennial-scale reduction produced by climate change alone.

Between sites, shore platform slope strongly modulates the suppression of wave breaking driven by coseismic subsidence. Shore platform slope controls how changes in nearshore water depth alter the location and occurrence of wave breaking. Broad, subhorizontal platforms provide an extensive shallow water zone across which breaking can shift landward as water levels rise. In contrast, steeper platforms have a narrower zone of wave transformation, such that rising water levels more readily allow waves to reach the cliff unbroken following subsidence. For earthquakes occurring in 2100, the median reduction in breaking and broken waves increases from 10.8% on subhorizontal platforms (< 1°), to 12.7 % on sloping platforms (1° to 5°) and 11.6% on steep platforms (> 5°). Maximum reductions in wave breaking similarly increase from 33.3% on subhorizontal platforms to 64.7% and 65.8% on sloping and steep platforms, respectively, relative to 2020 baseline conditions. Given this, shore-platform morphology controls not only how the offshore wave climate is filtered before reaching the coastline, but also each site's sensitivity to shifts in nearshore wave dynamics driven by megathrust earthquakes.

The reduction in breaking and broken waves is accompanied by a landward migration of wave breaking position. By the end of the century, for baseline model scenarios, median annual offshore wave breaking distances shift landward from 0 m to 185 m under SSP2-4.5 and 5 m to 245 m for SSP5-8.5, relative to 2020 breaking distances. Compared to no-earthquake conditions in the same year, coseismic subsidence under SSP-4.5 produces an additional, instantaneous landward shift with a median magnitude from 10 m for 0.5 m of subsidence to 25 m for 1.0 m and 40 m for 2.0 m, with maximum shifts of 193 m, 330 m, and 555 m, respectively. Under SSP5-8.5, the corresponding median shifts are 12.5 m, 25 m, and 40 m, with maxima of 190 m, 325 m, and 555 m. Based on these results, the landward migration of wave breaking is substantially more sensitive to coseismic subsidence magnitude than the background emissions trajectory. Increasing subsidence from 0.5 m to 2.0 m increases the median landward shift in wave breaking by 220 to 300%. By comparison, shifting from SSP2-4.5 to SSP5-8.5 increases the median shift by 25% under 0.5 m of subsidence, but not at all for 1.0 or 2.0 m of subsidence, reinforcing the overwhelming effect of the earthquake relative to the specific trajectory of climate change.

Increases in the magnitude of coseismic subsidence and in RSLR also coincide with shifts in which waves undergo breaking. For broken and breaking waves that occur during earthquake scenarios relative to the baseline scenarios for that same year, the median offshore wave height increases by up to 48% (1.4 m) across all sites and scenarios. The waves that continue to break under coseismic subsidence are larger and more energetic, delivering more power to the shore. Increasing the magnitude of coseismic subsidence also shifts the upper bounds of the median breaking and broken wave heights by 9.18% for 0.5 m subsidence, 19.10% for 1.0 m subsidence, and 48.29% for 2.0 m subsidence, across all sites and earthquake years relative to baseline conditions the same year.

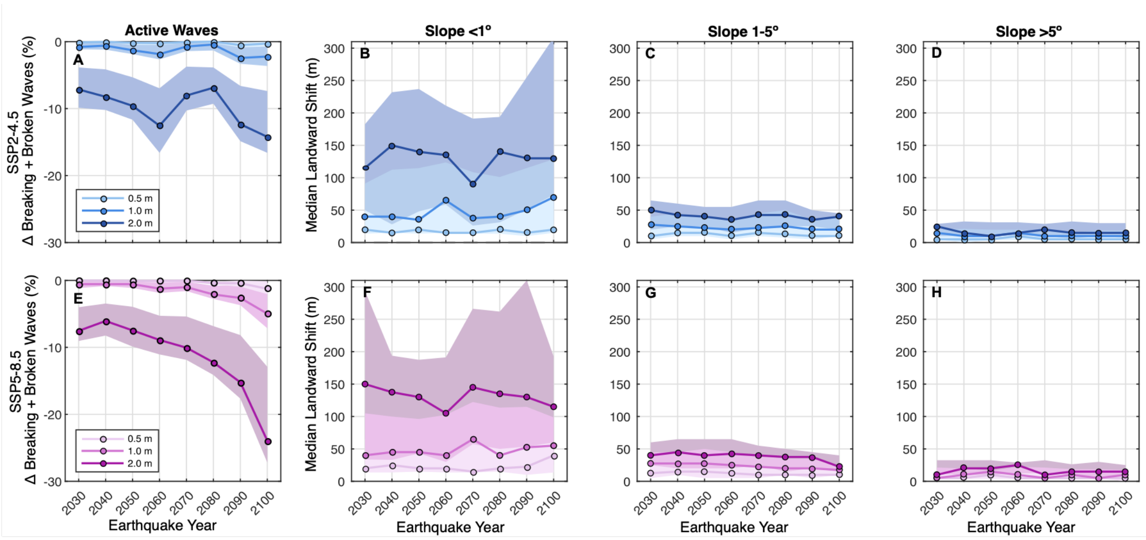

Figure 2. (A-B) Median percent change in the number of broken and breaking waves for SSP2-4.5 (A) and SS-5-8.5 (B) across each earthquake year and all sites, with shaded envelopes denoting the interquartile range. (C-G) Median landward shift in breaking distances across all sites by slope class for each earthquake year for SSP2-4.5 (C-E) and SSP5-8.5 (F-G). Shaded regions denote the interquartile range.

Subsidence-Driven Amplification of Cliff-Base Wave Power

Cliff-base wave power (P_{cliff}) is estimated for each forecast wave using a modified decay function (Materials and Methods; SI) to account for energy dissipation after breaking. The P_{cliff} estimates are then integrated over each year to calculate total annual P_{cliff}. We find that across all sites and scenarios, megathrust earthquake-driven subsidence drastically enhances wave power availability at shore. To further quantify the effects of earthquake-driven subsidence relative to baseline scenarios, we compute a P_{cliff} amplification factor defined as the ratio of P_{cliff} under an earthquake scenario to that under the baseline, SLR-only scenario for the same year (Methods and Materials).

The timing of maximum amplification, or the year in which a megathrust earthquake produces the greatest enhancement of P_{cliff} relative to baseline conditions, defines the upper envelope of earthquake-driven wave amplification. This timing is highly variable for a given earthquake across the model period, following emission scenario-specific patterns (Fig. 3A). Under SSP2-4.5, most sites demonstrate bimodal behavior, achieving maximum amplification during earthquakes that occur in 2030 or 2080. In contrast, under SSP5-8.5, amplification is greatest early in the model period around 2030 or 2040 before decreasing thereafter (Fig. 3A). For 0.5 m of subsidence, 7 sites feature the same maximum amplification years between SSP2-4.5 and SSP5-8.5 while 25 sites have different amplification years, 5 sites experience the same maximum amplification year for 1.0 m of subsidence, and 8 sites for 2.0 m of subsidence. This variability emphasizes the importance of the climate scenario in controlling the timing of maximum amplification.

For modeled earthquake scenarios under SSP2-4.5, maximum wave power amplification ranges from zero to a millionfold increase across all sites, scenarios, and years, which corresponds to a 10^1 to 10^4 kW/m increase in total annual P_{cliff}. Similarly, for SSP5-8.5, the maximum amplification of available P_{cliff} produces the same range of amplification factors. Overall, amplification scales with the magnitude of subsidence with the largest relative amplification occurring at sites with the low baseline P_{cliff} (Figure 3B-C). For 0.5 m of subsidence, maximum amplification ranges from 10^0 to 10^4 (10^0 to 10^3 kW/m), 10^0 to 10^5 (10^1 to 10^4 kW/m) for 1.0 m subsidence, and 10^0 to 10^6 (10^2 to 10^4 kW/m) for 2.0 m subsidence across all sites and scenarios relative to baseline, SLR-only conditions. These results also demonstrate a strong coupling between baseline P_{cliff} and the scale of amplification, such that sites with lower baseline P_{cliff} have higher amplification factors than those that already have high P_{cliff}. This indicates a strong and predictable relationship across climate scenarios, suggests that similar nearshore water levels set the magnitude of amplification.

Amplification also exhibits a strong dependence on shore platform morphology (Fig. 4). At each site across all model scenarios, mean P_{cliff} amplification is negatively correlated with shore platform slope (Spearman's $\rho \leq -0.91$, $p < 0.05$), indicating that earthquake-driven amplification is muted on steeper shore platforms. On subhorizontal shore platforms (< 1°), amplification ranges from 10^0 to 10^6 (10^0 to 10^3 kW/m). On sloping platforms, this range narrows by multiple orders of magnitude, to 10^0 to 10^2 (10^2 to 10^4 kW/m). Amplification is further reduced on steeply sloping platforms (> 5°) remaining within one order of magnitude, at 10^0 (10^3 to 10^4 kW/m). These results further demonstrate that site sensitivity to coseismic subsidence is strongly governed by nearshore morphology.

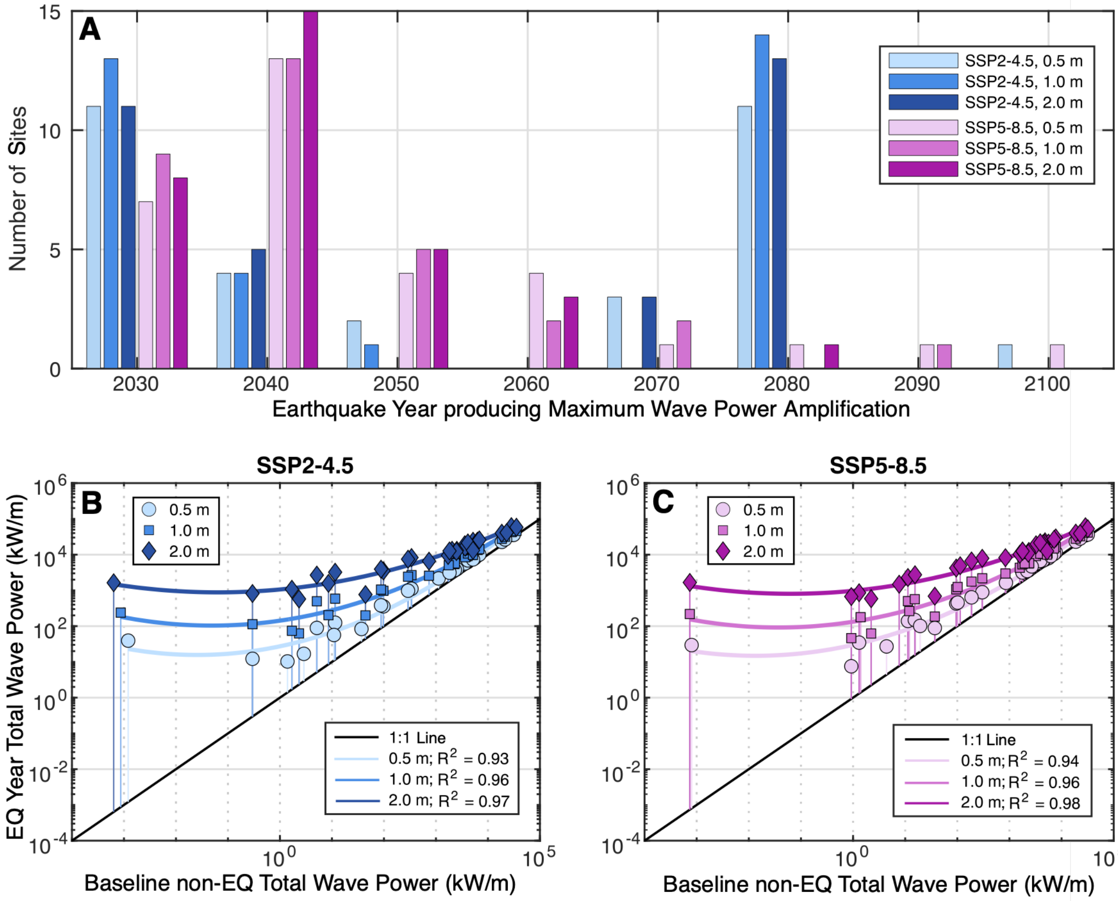

Figure 3. A) Earthquake years producing maximum amplification of wave power relative to a baseline scenario without coseismic subsidence. B-C) EQ year total annual P_{cliff} compared to baseline no EQ total annual P_{cliff} for site-specific EQ years that maximize amplification.

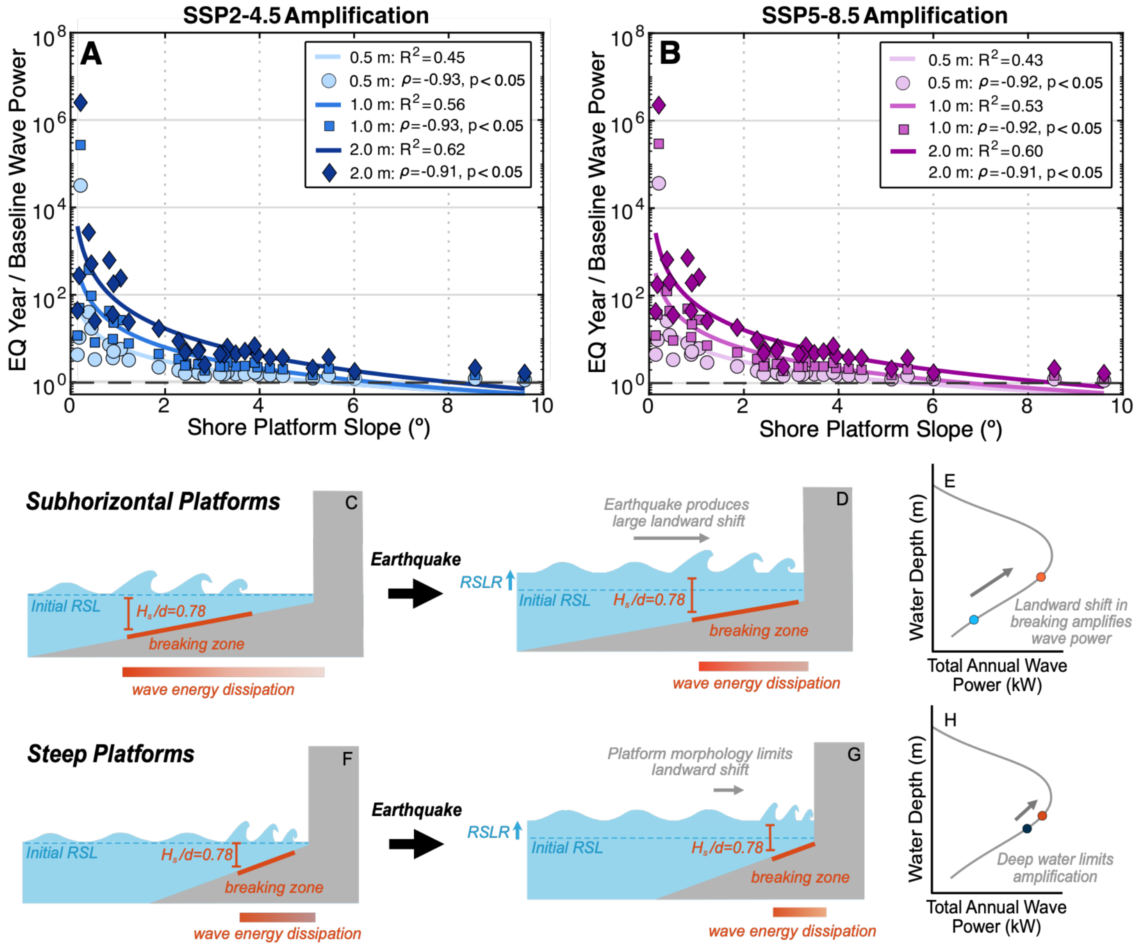

Figure 4. A-B). P_{cliff} amplification as a function of shore platform slope for site-specific EQ years that maximize wave power amplification. C-H) Schematic diagrams depicting the effects of earthquake driven RSLR on nearshore wave action and wave power for subhorizonal platforms (C-D) and steep platforms (F-H).

Seismic Memory and Coastal Hazard Trajectories

Megathrust earthquake-driven increases in nearshore water levels fundamentally changes the long-term trajectory of wave-energy forcing over the remainder of the century. Across all emissions-subsidence model pairings representing 256 unique scenarios spanning the full range of possible earthquake timings and magnitudes across all sites, increasing coseismic subsidence systematically shifts the timing of peak total annual P_{cliff} earlier in the century (Fig 5a). Under baseline, SLR-only conditions, the majority of simulations reach peak annual P_{cliff} near the end of the century, consistent with the increasing water depth associated with ongoing RSLR. However, as the magnitude of coseismic subsidence increases, a growing number of simulations achieve peak P_{cliff} earlier, with the largest subsidence scenarios exhibiting substantial clustering of peaks in P_{cliff} between 2070 to 2090, rather than 2100. This indicates that coseismic subsidence shifts the timing of peak P_{cliff} earlier by effectively accelerating the increases in wave power delivery that would otherwise occur more gradually through climate-driven SLR alone. Importantly, the years of peak total annual P_{cliff} do not coincide with the years that maximize amplification relative to baseline conditions. Instead, peaks in P_{cliff} are the result of the combined influence of earthquake-driven subsidence and RSLR, emphasizing that coastal wave-energy delivery depends on the evolving interaction between both processes rather than on the punctuated effects of the megathrust earthquake alone. Across all simulations where peak wave power is achieved before 2100, ~8% occur on subhorizontal shore platforms, ~58% on sloping shore platforms, and ~34% on steeply sloping sites, revealing a morphologic effect where the combination of steeper slopes and higher subsidence appear to shift peak cliff-incident wave power earlier.

Comparing total annual P_{cliff} in 2100 with that in the earthquake year across all model scenarios reveals how nearshore wave dynamics continue to evolve following coseismic subsidence (Fig. 5B). Ratios greater than one, which occur in 65.1% of model realizations, indicate that subsequent RSLR sustains or further amplifies the initial earthquake-driven increase in wave-energy delivery through 2100. An additional 12.5% of realizations have ratios equal to one, indicating no net change between the earthquake year and the end of the century. The remaining 22.4% have ratios less than one, indicating that wave power initially increases following coseismic subsidence but subsequently declines. Ratios below one occur across all shore platform slope classes, indicating that late-century declines are not restricted to a particular shore platform morphology. These contrasting trajectories reflect the nonlinear influence of water depth on nearshore wave transformation: although initial coseismic subsidence shifts wave breaking landward and increases energy delivery to the cliff across all sites and scenarios, in some instances continued RSLR can deepen water over the shore platform such that suppressed wave breaking can reduce P_{cliff}. Consequently, model runs combining greater coseismic subsidence with more severe emissions trajectories exhibit the lowest ratios and the greatest frequency of late-century declines. More rapid RSLR therefore mediates the post-earthquake recovery of the nearshore wave climate toward baseline conditions, driving a transition from enhanced to diminished wave-energy delivery over the decades following a megathrust earthquake.

To distinguish substantial declines in P_{cliff} from more minor year-to-year differences in wave climate, we identify all model realizations in which total annual P_{cliff} decreases by at least 5% between the earthquake year and 2100 (Fig. 5C). The magnitude of the post-peak decline, or lack thereof, is quantified as the fraction of model realizations in which total annual P_{cliff} decreases by at least 5% between P_{cliff} at the modeled earthquake year and 2100 (Fig. 5C). Under SSP2-4.5, the fraction of realizations exceeding this threshold increases from approximately 10% under 0.5 m of subsidence to 30% under 2.0 m. This sensitivity is substantially stronger under SSP5-8.5, where the fraction increases from approximately 20% to 70% across the same subsidence scenarios. Moreover, under SSP5-8.5 and 2.0 m of subsidence, 30% of realizations experience declines greater than 15%. These results demonstrate that more rapid late-century RSLR can progressively reverse the initial earthquake-driven amplification of wave power, making enhanced wave energy delivery increasingly transient as the magnitudes of both subsidence and subsequent sea-level rise increase.

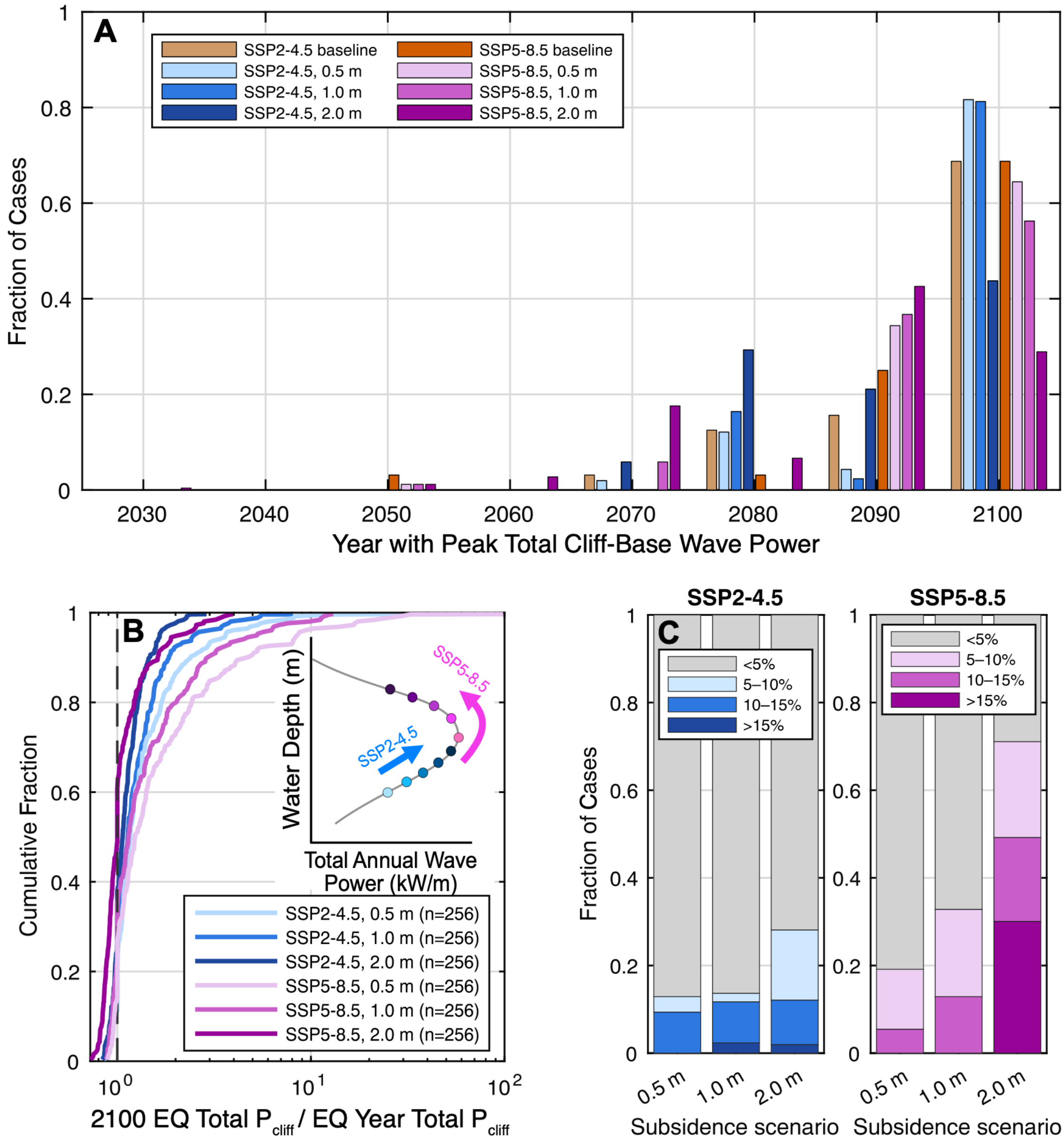

Figure 5. A) Year with peak total annual P_{cliff} (kW/m) for each coseismic subsidence, earthquake timing, and emissions scenario for all sites (n = 2048). B) Cumulative distribution of the ratio of P_{cliff} at 2100 to P_{cliff} for each earthquake year for all sites (n = 256). Inset schematically depicts the effects of subsidence on P_{cliff}. C) Fraction of model runs where P_{cliff} is reduced by 5% or more from peak total annual P_{cliff}, by subsidence scenario.

Discussion

Coseismic Subsidence and Sea Level Effects on Nearshore Wave Dynamics

Increasing coseismic subsidence and RSL decreases wave breaking in the nearshore (Fig. 2). These results agree with past studies (45) which find that as sea level rises, wave breaking decreases, suggesting reduced energy transfer to the shore and likely less erosion. Megathrust earthquake-driven subsidence produces this effect instantaneously, while also amplifying the sea level effects over time. We find that megathrust earthquake-driven subsidence and RSLR lead to hydrodynamic transitions in wave behavior, where water depth at the base of the shore becomes sufficiently deep to turn off wave breaking for some percentage of incident waves. At face value, this would suggest reduced energy at the cliff and therefore likely less erosion.

Coseismic subsidence changes not only whether waves break, but also where breaking occurs. The resulting increase in water depth produces an immediate landward migration of wave breaking. The magnitude of the shift reflects the interaction between coseismic subsidence and shore-platform slope, where greater subsidence produces greater shifts in nearshore water depth. Gently sloping platforms translate this shift into a much larger landward migration of wave breaking relative to steeply sloping platforms. In this way, the translation of coseismic subsidence to shifts in wave energy delivery at any individual site depends strongly on shore platform morphology.

However, model simulations show that P_{cliff} increases with coseismic subsidence and RSLR despite the accompanying reduction in wave breaking. This apparent contradiction reflects a competition between two effects: the loss of waves from the breaking-wave population and the landward migration of the waves that continue to break. Increasing water depth preferentially suppresses the breaking of smaller, lower-energy waves, shifting the remaining breaking-wave population toward the higher-energy portion of the offshore wave distribution. At the same time, larger waves continue to break but do so progressively closer to the coastline. Because these waves traverse a shorter distance through the nearshore after breaking, they dissipate less energy before reaching the cliff. In our simulations, this reduction in energy loss outweighs the removal of smaller waves from the breaking-wave population, producing a net increase in total P_{cliff}. This interpretation assumes a constant rate of wave-energy dissipation across all 32 rocky coast sites explored in this study (Methods and Materials; SI). In natural settings, shore platform energy dissipation rates may vary with platform geometry, roughness, and substrate conditions (70–73). However, these effects remain poorly constrained in current treatments of nearshore wave transformation. Our results emphasize that wave-energy delivery depends not only on the fraction and power distribution of waves that break, but also on where breaking occurs and how much energy those waves retain while traversing the nearshore.

This competition between the loss of breaking waves and the landward migration of wave breaking has implications beyond Cascadia. This same mechanism should operate along rocky coastlines wherever abrupt or gradual RSLR increases water depth over a shore platform. Hazard assessments and predictions of coastal cliff retreat based only on the prevalence of breaking waves may therefore underestimate erosion hazards by overlooking changes in breaking location, the energy distribution of the remaining breaking waves, and the distance over which that energy is dissipated (74, 75). Predicting rocky coast response to earthquake-driven coseismic subsidence and sea level rise requires accounting for these interacting controls on wave energy delivery rather than treating reduced wave breaking as evidence of reduced erosional potential on rocky coasts.

Emissions Trajectory Controls the Timing and Magnitude of Earthquake-Driven Wave Amplification

Our results suggest an earthquake-climate coupling that governs the timing of maximum amplification and peak P_{cliff}. Coseismic subsidence establishes the magnitude of the abrupt increase in water depth, but the emissions-dependent sea-level trajectory determines when this perturbation produces its greatest amplification of P_{cliff} (Fig. 3). Under SSP2-4.5, maximum amplification generally occurs later in the century, around 2070–2080. However, because the slower rise in sea level produces a weaker temporal trend, interannual variability in the projected offshore wave climate exerts a stronger influence on the timing of maximum earthquake-driven amplification. Under SSP5-8.5, by contrast, the strongest amplification is associated with earthquakes occurring earlier in the century. As rapid sea level rise progressively deepens the nearshore, it also suppresses the additional wave-power amplification produced by a late-century Cascadia megathrust earthquake. High emissions therefore both advance the period of maximum earthquake sensitivity and diminish the relative impact of earthquakes occurring near the end of the century. These results demonstrate that identical earthquake events may produce significantly different coastal impacts depending on the background sea level and climate state when they occur.

Importantly, coseismic subsidence consistently increases P_{cliff} relative to equivalent scenarios without an earthquake. The timing and persistence of that amplification, however, differs strongly between emissions scenarios. Our results reveal that earthquake- and climate-driven changes in coastal wave hazards are not simply additive. Rather, their interaction creates a time-dependent period of enhanced wave forcing governed by the emissions trajectory. Under SSP5-8.5, rapid sea-level rise initially promotes greater energy delivery but also advances the hydrodynamic transition at which deeper water suppresses wave breaking and reduces the additional power delivered to the cliff. Consequently, the window of maximum earthquake-driven amplification occurs earlier under SSP5-8.5 than under SSP2-4.5. The high-emissions trajectory not only shifts the timing of the earthquake that stands to have the most profound impact on coastal hazards but further increases the likelihood that peak wave forcing will occur decades before 2100 (Fig. 5). Following a megathrust earthquake, our results show that continued sea level rise can drive a partial recovery of the nearshore wave climate toward baseline conditions as progressive deepening suppresses wave breaking and diminishes the initial amplification of P_{cliff}. This recovery is most pronounced under SSP5-8.5, indicating that more rapid sea-level rise may help to mediate the wave energy amplification driven by the next Cascadia megathrust by the end of the century. The greatest wave-erosion hazard does not necessarily coincide with the highest sea level and may occur decades before the end of the century. By identifying this climate-dependent window for maximized coastal hazards, our results provide a new framework for predicting how strongly rocky coastlines respond to megathrust earthquakes through time.

It is important to note, however, that SSP5-8.5 is increasingly regarded as a relatively unlikely high emissions pathway rather than the most probable climate future (76, 77). The post-earthquake recovery of nearshore wave climate suggested by our model results should therefore be interpreted as an upper-bound response to rapid sea level rise. By contrast, SSP2-4.5 produces a more variable response across sites, a lower likelihood of nearshore wave climate recovery, and less predictable impacts for earthquakes occurring at different times. Our analysis is constrained by the availability of internally consistent projections of both future sea levels and offshore wave climates. Because SSP5-8.5 provides an upper bound on future sea-level rise, the slower rise expected under more likely climate futures may be less effective at consistently suppressing earthquake-driven amplification. Local morphology, earthquake timing, and interannual wave variability may therefore exert stronger controls on the response at individual sites. Sustained enhancement of wave-energy delivery and its associated erosion hazard may consequently be more likely, but also more spatially and temporally variable compared to results presented here using SSP5-8.5.

Further, the reduced P_{cliff} amplification under a high emissions future should not be interpreted as a corresponding reduction in overall coastal hazard. The same increases in water depth that suppress wave breaking and promote post-earthquake recovery of the nearshore wave climate also increase exposure to coastal inundation (8, 78, 79). More rapid sea-level rise may therefore shift the dominant post-earthquake hazard from intensified wave-driven erosion toward more persistent inundation, particularly where coseismic subsidence abruptly lowers the coastline. Conversely, slower, more plausible sea-level trajectories may sustain enhanced wave-driven erosion over longer periods. The apparent recovery of P_{cliff} consequently represents a redistribution of coastal hazards rather than a return to pre-earthquake conditions.

Although the magnitude of coseismic deformation modeled here is specific to Cascadia, the underlying mechanism should extend to rocky coastlines wherever tectonic subsidence, gradual sea-level rise, or both alter water depth over a shore platform. The translation of these effects to coastal wave power will strongly depend on platform slope and width, as well as offshore wave climate and tidal range. This study provides a transferable framework for identifying coastlines where rising water levels may initially amplify wave-driven erosion, but later suppress wave-energy delivery, simultaneously increasing inundation exposure. More broadly, our results demonstrate that future rocky coast hazards are amplified under the interaction of solid-Earth deformation and climate-driven sea-level rise.

The Geomorphic Legacy of Megathrust Earthquakes: Implications for Coastal Erosion and Future Hazards

Coastal erosion and shoreline retreat are regulated by the wave power delivered to the coastline. Consequently, on rocky coasts, increases in P_{cliff} driven by coseismic subsidence and RSLR are expected to enhance coastal erosion, relative to the scenarios without earthquakes. However, increases in erosion are unlikely to be spatially uniform across the region. This is because local shore platform morphology strongly regulates the magnitude of amplification. On steeply sloping sites, earthquake-driven amplification is relatively subdued, leading to only modest increases (Fig. 4). However, on sub-horizontal and lower sloping shore platforms, coseismic subsidence can amplify P_{cliff} by substantial amounts (Fig. 4). Over longer timescales, rocky coast retreat rates scale with mean annual wave power, such that an order-of-magnitude increase in wave power drives a roughly proportional increase in retreat rate (35). Although extrapolating this relationship across significant changes remains uncertain, multiple orders of magnitude amplifications in P_{cliff} are likely to fundamentally alter the prevailing wave-driven erosion regime following the next Cascadia megathrust earthquake. These results identify gently sloping shore platforms as potential hot spots of earthquake-driven acceleration of coastal cliff retreat. Further, they highlight how a spatially extensive tectonic event may be translated into highly variable local geomorphic change.

Importantly, our results suggest that coseismic subsidence produces a persistent shift in the nearshore wave energy regime over the model period. Although continued RSLR can drive partial recovery of the nearshore wave climate toward baseline conditions in some locations, P_{cliff} remains elevated in most model instances because the coseismic elevation offset is not recovered. It is worth noting that this persistence depends, in part, on the treatment of postseismic vertical land motion. The postseismic phase of the seismic cycle is governed primarily by viscoelastic relaxation in the lower crust and upper mantle, with additional contributions from afterslip (80–84). Vertical deformation associated with this phase remains poorly constrained in the CSZ. Observations and geophysical modeling from other subduction zones indicate both relatively rapid recovery of coseismic deformation (88, 89) and shifts in coastal erosion (90), and more minor viscoelastic relaxation driven deformation (91, 92). Due to this uncertainty, we do not explicitly incorporate vertical postseismic deformation rates or behavior into the model. Instead, following coseismic displacement, vertical land motion rates are reset to the interseismic values for all subsequent time steps. This produces irrecoverable enhancement of P_{cliff}, but rapid uplift in the years to decades following a megathrust earthquake could potentially allow a return to initial conditions earlier, even during the model period. However, how the added effect of SLR plays into this dynamic remains an avenue for future research.

Our results suggest that the earthquake cycle may partition coastal retreat between prolonged interseismic erosion and shorter, more intense pulses of post-earthquake change. Interseismic periods persist for centuries and may therefore account for a substantial fraction of cumulative erosion even at comparatively modest rates. Coseismic subsidence is effectively instantaneous, but the resulting orders-of-magnitude increases in P_{cliff} can persist for decades at some gently sloping sites, potentially concentrating a disproportionate share of total retreat within the period following a megathrust earthquake. The relative contribution of interseismic and post-earthquake rocky coast erosion will depend on both the magnitude and duration of wave-power at a given site, as well as the underlying relationship between wave power and retreat rate. At steep sites, modest amplification may leave interseismic erosion dominant, whereas at gently sloping sites, relatively brief but more extreme post-earthquake wave forcing could dominate the long-term retreat budget. Although the present model does not calculate this partitioning directly, coupling these results with process-based erosion models offers a path toward determining whether rocky coastlines evolve primarily through persistent interseismic erosion or episodic pulses of post-earthquake retreat (36, 93–95).

This partitioning of erosion across the earthquake cycle is also likely to differ among tectonic settings. Cascadia represents a subsidence-dominated end member (5, 96, 97) in which coseismic deformation increases nearshore water depth and amplifies wave-energy delivery. Earthquakes on other fault systems – including transpressional segments of strike-slip systems such as the San Andreas Fault and New Zealand's Marlborough Fault System – can instead produce coastal uplift that raises shore platforms and shifts wave attack seaward (98–100) . Indeed, following the 2016 Kaikōura earthquake, approximately 1 m of coseismic uplift reduced incident onshore wave energy by nearly 40% and disconnected much of the former intertidal platform from wave erosion, initially buffering the cliff and promoting formation of an incipient marine terrace. These contrasting responses suggest that earthquakes can either accelerate or suppress wave-driven retreat depending on the direction and spatial pattern of vertical land motion.

Rocky coast retreat is governed by highly episodic cliff failures rather than continuous erosion. The exact magnitude and timing of cliff failure remains poorly constrained due to interactions between marine and subaerial environmental forcing, geology, and structural controls (101–103). This uncertainty is especially consequential in Cascadia, where coastal communities and critical infrastructure are commonly concentrated along or immediately landward of eroding cliffs. Earthquake-driven increases in wave forcing could therefore compound the immediate effects of ground shaking, coseismic subsidence, and tsunami inundation wit elevated erosion hazards that persists for decades.

Nevertheless, measured shoreline retreat rates in the region (104–106) and observed scaling relationships between wave power and erosion rates (34, 35), strongly suggest that the modeled multiple order of magnitude increases in cliff wave power will accelerate cliff retreat, specifically on sub-horizontal and low sloping sites. Whether this enhanced forcing produces more frequent incremental failures, catastrophic collapse, or delayed failure following progressive weakening remains unknown (107). Coupling wave transformation and cliff failure models (108) with direct coastal monitoring though satellite altimetry (109), cliff-top seismometers, and repeat lidar scans (110–114) provides a potential path forward towards resolving these responses. Monitoring initiated before the next Cascadia earthquake will be particularly valuable because it can establish the baseline needed to quantify how rapidly cliff erosion responds and how long the geomorphic effects persist. Incorporating these longer-lived erosion hazards into post-earthquake recovery and infrastructure planning will be essential for anticipating the coastal hazard cascade following the next Cascadia megathrust earthquake.

While this study specifically focuses on the Cascadia Subduction Zone, the solid Earth-climate coupling we identify has global implications for future hazard potential along tectonically active margins (115–117). The framework developed here provides a basis for predicting where earthquakes will produce sustained erosion, transient amplification followed by recovery, or an immediate reduction in wave attack following uplift. Accordingly, hazard management and planning should incorporate the potential effects of these multi-hazards to ensure proper preparedness and response not in the immediate aftermath of an earthquake, but in the decades that follow (118). More broadly, incorporating the complete earthquake cycle into models of rocky-coast evolution will be essential for understanding how tectonic and climatic forcing interact to shape coastal hazards and landscapes.

Materials and Methods

To evaluate the integrated and varying effects of coseismic subsidence and RSLR on nearshore wave dynamics, we select 32 sites comprising rocky cliffs and bluffs across the length of the CSZ (Fig. 1) dominated by offshore deepwater wave climates (49, 50). Hourly model simulations are run from 2020 – 2100 for two climate scenarios; SSP2-4.5 and SSP5-8.5, which provide lower and upper bounds corresponding to intermediate and high trajectories. These scenarios were selected because SSP2-4.5 represents the lower limit of likely emissions trajectories while SSP5-8.5 serves as an extreme, high-emissions upper bound (51).

We utilize IPCC AR6 regional, medium-confidence sea level projections for the corresponding emissions scenarios in this study. We adopt the 50th percentile projections and extract the nearest sea level curve for each study site from the underlying 1° resolution dataset (51–53). The accumulation of strain along the coupled zone of the fault during the interseismic period drives vertical land motion, with additional contributions and effects from glacial isostatic adjustment and fault creep at depth (54–57). The combined effect of these processes are expressed in vertical land motion rates derived from local tide gauge sea level records, which also account for eustatic sea level trends (58). Annual rates are converted to hourly rates and applied at each model time-step. Because we independently account for this deformation in the model, we use sea level curves from which the vertical land motion contributions have been removed to avoid overestimating these effects.

Tidal influences on coastal water levels are accounted for by incorporating predicted hourly water levels referenced to a mean sea level datum derived from harmonic analysis at the nearest tidal station for each site for the model period .

Offshore wave power is determined for each site from hourly 1º deep-water wave forecasts of significant wave heights and energy periods for the corresponding RCP emission scenario (46). To account for local nearshore morphology and energy dissipation, we extract 1/2 km wide swath profiles along the prevailing wave direction from 1/3 arc-second resolution bathymetric data sets which we interpolate to a 5m resolution (60). Linear wave theory is subsequently utilized to model wave transformations associated with shallow-water propagation to identify where conditions for the depth-dependent breaking criterion ($\gamma = 0.78$) are satisfied for the entire distribution of forecast wave measurements (SI).

Based on the water level that coincides with shore incident waves and their breaking distance relative to the coastal cliff, waves can be classified based on impact type (breaking, broken, or unbroken) in accordance with Matsumoto et al., 2024. Breaking waves transfer the most energy because they break right at the cliff, while the amount of energy or power delivered by broken waves depends on the offshore breaking distance, which is modulated by wave size, coastal morphology, and cliff-base water levels. For unbroken waves, we assume negligible cliff wave power because these waves are reflected off the cliff face without breaking (61, 62). Additionally, cliff-base wave power is estimated using a modified decay function (63–65):

$$P_{cliff} = P_{breaking} e^{-k \cdot d} \qquad (1)$$

Where k (m^{-1}) is an attenuation constant, representing the wave dissipation rate and d is the wave breaking distance, defined at the position where depth-dependent breaking criterion is met. Three different constants are utilized (0.01, 0.05, 0.1), for each cliff wave power calculation, representing low, medium, and high attenuation respectively.

We systematically vary both the magnitude (0.5 m, 1.0 m, and 2.0 m) and timing (2030, 2040, 2050, 2060, 2070, 2080, 2090, and 2100) of coseismic subsidence. In addition, we include a control scenario without earthquake-induced subsidence to isolate the effects of RSLR in the absence of coseismic deformation. Earthquake driven subsidence (or lack thereof) is the only differentiating factor between these scenarios, all other processes and model inputs remain the same, thus the baseline, SLR-only scenario still accounts for interseismic VLM.

These model simulations are conducted for both emission scenarios at each study site. We run a total of 25 different simulations for each site per climate scenario for 1600 total model runs (800 runs across each climate scenario).

To quantify the effects of earthquake driven subsidence relative to the scenario without any coseismic subsidence, we calculate a wave power amplification factor (-). This is a ratio between the total annual P_{cliff} of a given year for a scenario with an earthquake and the same metric for the same year but for a baseline, SLR-only scenario:

$$Amplification\ Factor = \frac{Total\ Annual\ P_{cliff}\ for\ EQ\ Scenario}{Baseline\ SLR\ only\ Total\ Annual\ P_{cliff}}$$

Our model assumes that wave energy is conserved up to the point of breaking, neglecting dissipation during shoaling, as the majority of energy loss occurs during the breaking process (66–68). Additionally, we do not incorporate shallow-water processes such as wave setup, reflection, refraction, or diffraction. This simplification reflects our primary objective of isolating and characterizing the effects of RSLR on nearshore energy transfer, rather than to comprehensively model all aspects of shallow-water wave dynamics. This approach is consistent with prior wave modeling studies. The model also does not account for any changes to coastal morphology other than vertical movement of the cross-shore profile. Given the short timescale of the model simulations (80 years), the fact that we do not estimate coastal erosion rates, and the lithological composition of our study sites, this is a reasonable choice. Nonetheless, events like cliff failure or rapid shoreline retreat could lead to changes in cliff-base wave energy regimes which the model cannot account for.

Acknowledgments

This study was supported by National Science Foundation grant 2339542 awarded to CCM. We are grateful to Kimberly Huppert, Roger Michaelides, and Doug Wiens for thoughtful discussions which contributed to the development of this work.

Competing interests: The authors declare no competing interest.

References

1. M. G. Bostock, N. I. Christensen, S. M. Peacock, Seismicity in Cascadia. *Lithos* **332–333**, 55–66 (2019).

2. J. D. Chaytor, C. Goldfinger, R. P. Dziak, C. G. Fox, Active deformation of the Gorda plate: Constraining deformation models with new geophysical data. *Geol* **32**, 353 (2004).

3. S. P. S. Gulick, A. S. Meltzer, T. J. Henstock, A. Levander, Internal deformation of the southern Gorda plate: Fragmentation of a weak plate near the Mendocino triple junction. *Geol* **29**, 691 (2001).

4. P. A. McCrory, J. L. Blair, F. Waldhauser, D. H. Oppenheimer, Juan de Fuca slab geometry and its relation to Wadati-Benioff zone seismicity. *J. Geophys. Res.* **117**, 2012JB009407 (2012).

5. M. A. L. Walton, *et al.*, Toward an Integrative Geological and Geophysical View of Cascadia Subduction Zone Earthquakes. *Annual Review of Earth and Planetary Sciences* **49**, 367–398 (2021).

6. S. L. Bilek, T. Lay, Subduction zone megathrust earthquakes. *Geosphere* **14**, 1468–1500 (2018).

7. M. D. Petersen, C. H. Cramer, A. D. Frankel, Simulations of Seismic Hazard for the Pacific Northwest of the United States from Earthquakes Associated with the Cascadia Subduction Zone. *Pure and Applied Geophysics* **159**, 2147–2168 (2002).

8. T. Dura, *et al.*, Increased flood exposure in the Pacific Northwest following earthquake-driven subsidence and sea-level rise. *Proc. Natl. Acad. Sci. U.S.A.* **122**, e2424659122 (2025).

9. T. H. Heaton, S. H. Hartzell, Earthquake Hazards on the Cascadia Subduction Zone. *Science* **236**, 162–168 (1987).

10. C. Goldfinger, *et al.*, The importance of site selection, sediment supply, and hydrodynamics: A case study of submarine paleoseismology on the northern Cascadia margin, Washington USA. *Marine Geology* **384**, 4–46 (2017).

11. A. R. Nelson, *et al.*, A maximum rupture model for the central and southern Cascadia subduction zone—reassessing ages for coastal evidence of megathrust earthquakes and tsunamis. *Quaternary Science Reviews* **261**, 106922 (2021).

12. G. C. Jacoby, D. E. Bunker, B. E. Benson, Tree-ring evidence for an A.D. 1700 Cascadia earthquake in Washington and northern Oregon. *Geol* **25**, 999 (1997).

13. K. Satake, K. Shimazaki, Y. Tsuji, K. Ueda, Time and size of a giant earthquake in Cascadia inferred from Japanese tsunami records of January 1700. *Nature* **379**, 246–249 (1996).

14. M. D. Petersen, *et al.*, The 2018 update of the US National Seismic Hazard Model: Overview of model and implications. *Earthquake Spectra* **36**, 5–41 (2020).

15. E. A. Wirth, *et al.*, "Earthquake Probabilities and Hazards in the U.S. Pacific Northwest" (US Geologic Survey, 2025).

16. B. F. Atwater, Evidence for Great Holocene Earthquakes Along the Outer Coast of Washington State. *Science* **236**, 942–944 (1987).

17. A. D. Hawkes, B. P. Horton, A. R. Nelson, C. H. Vane, Y. Sawai, Coastal subsidence in Oregon, USA, during the giant Cascadia earthquake of AD 1700. *Quaternary Science Reviews* **30**, 364–376 (2011).

18. A. C. Kemp, N. Cahill, S. E. Engelhart, A. D. Hawkes, K. Wang, Revising Estimates of Spatially Variable Subsidence during the A.D. 1700 Cascadia Earthquake Using a Bayesian Foraminiferal Transfer Function. *Bulletin of the Seismological Society of America* **108**, 654–673 (2018).

19. L. J. Leonard, C. A. Currie, S. Mazzotti, R. D. Hyndman, Rupture area and displacement of past Cascadia great earthquakes from coastal coseismic subsidence. *Geological Society of America Bulletin* **122**, 2079–2096 (2010).

20. L. J. Leonard, R. D. Hyndman, S. Mazzotti, Coseismic subsidence in the 1700 great Cascadia earthquake: Coastal estimates versus elastic dislocation models. *Geo. Society Am. Bull.* **116**, 655 (2004).

21. A. R. Nelson, I. Shennan, A. J. Long, Identifying coseismic subsidence in tidal-wetland stratigraphic sequences at the Cascadia subduction zone of western North America. *J. Geophys. Res.* **101**, 6115–6135 (1996).

22. A. M. Dunham, *et al.*, The Impact of 3D Structure on Coseismic Coastal Land-Level Change and Tsunami Generation in the Cascadia Subduction Zone. *Geophysical Research Letters* **52**, e2025GL117783 (2025).

23. D. Melgar, Was the January 26th, 1700 Cascadia Earthquake Part of a Rupture Sequence? *JGR Solid Earth* **126**, e2021JB021822 (2021).

24. D. T. Small, D. Melgar, Geodetic Coupling Models as Constraints on Stochastic Earthquake Ruptures: An Example Application to PTHA in Cascadia. *JGR Solid Earth* **126**, e2020JB021149 (2021).

25. E. A. Wirth, A. D. Frankel, Impact of Down-Dip Rupture Limit and High-Stress Drop Subevents on Coseismic Land-Level Change during Cascadia Megathrust Earthquakes. *Bulletin of the Seismological Society of America* **109**, 2187–2197 (2019).

26. A. Rovere, P. Stocchi, M. Vacchi, Eustatic and Relative Sea Level Changes. *Curr Clim Change Rep* **2**, 221–231 (2016).

27. D. Melini, *et al.*, Earthquakes and relative sealevel changes. *Geophysical Research Letters* **31**, 2003GL019347 (2004).

28. T. Frederikse, *et al.*, The causes of sea-level rise since 1900. *Nature* **584**, 393–397 (2020).

29. B. D. Hamlington, *et al.*, The rate of global sea level rise doubled during the past three decades. *Commun Earth Environ* **5**, 601 (2024).

30. R. S. Nerem, *et al.*, Climate-change–driven accelerated sea-level rise detected in the altimeter era. *Proc. Natl. Acad. Sci. U.S.A.* **115**, 2022–2025 (2018).

31. P. D. Komar, J. C. Allan*, P. Ruggiero, Sea Level Variations along the U.S. Pacific Northwest Coast: Tectonic and Climate Controls. *Journal of Coastal Research* **276**, 808–823 (2011).

32. Intergovernmental Panel On Climate Change (Ipcc), *The Ocean and Cryosphere in a Changing Climate: Special Report of the Intergovernmental Panel on Climate Change*, 1st Ed. (Cambridge University Press, 2022).

33. Intergovernmental Panel On Climate Change (Ipcc), *Climate Change 2021 – The Physical Science Basis: Working Group I Contribution to the Sixth Assessment Report of the Intergovernmental Panel on Climate Change*, 1st Ed. (Cambridge University Press, 2023).

34. P. Alessio, E. A. Keller, Short-term patterns and processes of coastal cliff erosion in Santa Barbara, California. *Geomorphology* **353**, 106994 (2020).

35. K. L. Huppert, J. T. Perron, A. D. Ashton, The influence of wave power on bedrock sea-cliff erosion in the Hawaiian Islands. *Geology* **48**, 499–503 (2020).

36. C. G. Lopez, C. C. Masteller, Tectonics as a Regulator of Shoreline Retreat and Rocky Coast Evolution Across Timescales. *AGU Advances* **7**, e2025AV002065 (2026).

37. D. M. Gilford, J. Giguere, A. J. Pershing, Human-caused ocean warming has intensified recent hurricanes. *Environ. Res.: Climate* **3**, 045019 (2024).

38. A. Meucci, I. R. Young, M. Hemer, C. Trenham, I. G. Watterson, 140 Years of Global Ocean Wind-Wave Climate Derived from CMIP6 ACCESS-CM2 and EC-Earth3 GCMs: Global Trends, Regional Changes, and Future Projections. *Journal of Climate* **36**, 1605–1631 (2023).

39. B. G. Reguero, I. J. Losada, F. J. Méndez, A recent increase in global wave power as a consequence of oceanic warming. *Nat Commun* **10**, 205 (2019).

40. I. R. Young, A. Ribal, Multiplatform evaluation of global trends in wind speed and wave height. *Science* **364**, 548–552 (2019).

41. P. W. Limber, P. L. Barnard, S. Vitousek, L. H. Erikson, A Model Ensemble for Projecting Multidecadal Coastal Cliff Retreat During the 21st Century. *JGR Earth Surface* **123**, 1566–1589 (2018).

42. J. R. Shadrick, *et al.*, Sea-level rise will likely accelerate rock coast cliff retreat rates. *Nat Commun* **13**, 7005 (2022).

43. A. S. Trenhaile, Predicting the response of hard and soft rock coasts to changes in sea level and wave height. *Climatic Change* **109**, 599–615 (2011).

44. M. E. Dickson, *et al.*, Sea-level rise may not uniformly accelerate cliff erosion rates. *Nat Commun* **14**, 8485 (2023).

45. H. Matsumoto, M. E. Dickson, W. J. Stephenson, C. F. Thompson, A. P. Young, Modeling future cliff-front waves during sea level rise and implications for coastal cliff retreat rates. *Sci Rep* **14**, 7810 (2024).

46. L. M. Bricheno, J. Wolf, RisesAM-OceanWaves: An hourly simulation of sea surface waves for historic and future climate. NERC EDS British Oceanographic Data Centre NOC. Deposited 2023.

47. R. Kirk, *et al.*, “Shore Platforms” in *Encyclopedia of Coastal Science*, M. L. Schwartz, Ed. (Springer Netherlands, 2005), pp. 873–875.

48. T. Sunamura, *Geomorphology of Rocky Coasts* (J. Wiley, 1992).

49. K. Tillotson, P. D. Komar, The Wave Climate of the Pacific Northwest (Oregon and Washington): A Comparison of Data Sources. *Journal of Coastal Research* **13**, 440–452 (1997).

50. Z. Yang, *et al.*, Modeling analysis of the swell and wind-sea climate in the Salish Sea. *Estuarine, Coastal and Shelf Science* **224**, 289–300 (2019).

51. Intergovernmental Panel On Climate Change (Ipcc), *Climate Change 2021 – The Physical Science Basis: Working Group I Contribution to the Sixth Assessment Report of the Intergovernmental Panel on Climate Change*, 1st Ed. (Cambridge University Press, 2023).

52. G. G. Garner, *et al.*, IPCC AR6 Sea Level Projections. Zenodo. https://doi.org/10.5281/ZENODO.5914709. Deposited 9 August 2021.

53. R. E. Kopp, *et al.*, The Framework for Assessing Changes To Sea-level (FACTS) v1.0: a platform for characterizing parametric and structural uncertainty in future global, relative, and extreme sea-level change. *Geosci. Model Dev.* **16**, 7461–7489 (2023).

54. R. J. Burgette, R. J. Weldon, D. A. Schmidt, Interseismic uplift rates for western Oregon and along-strike variation in locking on the Cascadia subduction zone. *J. Geophys. Res.* **114**, 2008JB005679 (2009).

55. J. Clark, J. X. Mitrovica, K. Latychev, Glacial isostatic adjustment in central Cascadia: Insights from three-dimensional Earth modeling. *Geology* **47**, 295–298 (2019).

56. G. M. Schmalzle, R. McCaffrey, K. C. Creager, Central Cascadia subduction zone creep. *Geochem. Geophys. Geosyst.* **15**, 1515–1532 (2014).

57. K. M. Stanton, J. G. Crider, H. M. Kelsey, J. K. Feathers, The signature of accumulated permanent uplift, northern Cascadia subduction zone. *Quat. res.* **117**, 98–118 (2024).

58. C. E. Zervas, S. K. Gill, W. (William V. Sweet, Estimating vertical land motion from long-term tide gauge records. (2013).

59. NOAA Tides and Currents. Available at: https://tidesandcurrents.noaa.gov/ [Accessed 6 August 2025].

60. NOAA National Centers for Environmental Information, Coastal Relief Models (CRMs). NOAA National Centers for Environmental Information. https://doi.org/10.25921/5ZN5-KN44. Deposited 2023.

61. G. N. Bullock, C. Obhrai, D. H. Peregrine, H. Bredmose, Violent breaking wave impacts. Part 1: Results from large-scale regular wave tests on vertical and sloping walls. *Coastal Engineering* **54**, 602–617 (2007).

62. C. F. Thompson, A. P. Young, M. E. Dickson, Wave impacts on coastal cliffs: Do bigger waves drive greater ground motion? *Earth Surface Processes and Landforms* **44**, 2849–2860 (2019).

63. A. S. Trenhaile, Modeling the development of wave-cut shore platforms. *Marine Geology* **166**, 163–178 (2000).

64. A. Trenhaile, Modelling the development of dynamic equilibrium on shore platforms. *Marine Geology* **427**, 106227 (2020).

65. C. Arróspide, H. Carrillo, G. Aguilar, R. Cienfuegos, A numerical model for wave erosion spatial variability at a Headland-Bay scale on rock coasts: Development and testing with synthetic and measured bathymetries. *Marine Geology* **489**, 107634 (2025).

66. A. V. Babanin, K. N. Tsagareli, I. R. Young, D. J. Walker, Numerical Investigation of Spectral Evolution of Wind Waves. Part II: Dissipation Term and Evolution Tests. *Journal of Physical Oceanography* **40**, 667–683 (2010).

67. J. R. Gemmrich, T. D. Mudge, V. D. Polonichko, On the Energy Input from Wind to Surface Waves. *J. Phys. Oceanogr.* **24**, 2413–2417 (1994).

68. A. Iafrati, Energy dissipation mechanisms in wave breaking processes: Spilling and highly aerated plunging breaking events. *J. Geophys. Res.* **116**, 2011JC007038 (2011).

69. H. Matsumoto, M. E. Dickson, P. S. Kench, Modelling the Development of Varied Shore Profile Geometry on Rocky Coasts. *Journal of Coastal Research* **75**, 597–601 (2016).

70. W. J. Stephenson, L. A. Naylor, H. Smith, B. Chen, R. P. Brayne, Wave transformation across a macrotidal shore platform under low to moderate energy conditions. *Earth Surf Processes Landf* **43**, 298–311 (2018).

71. T. Poate, G. Masselink, M. J. Austin, M. Dickson, R. McCall, The Role of Bed Roughness in Wave Transformation Across Sloping Rock Shore Platforms. *JGR Earth Surface* **123**, 97–123 (2018).

72. R. J. E. Marshall, W. J. Stephenson, The morphodynamics of shore platforms in a micro-tidal setting: Interactions between waves and morphology. *Marine Geology* **288**, 18–31 (2011).

73. H. Ogawa, M. E. Dickson, P. S. Kench, Wave transformation on a sub-horizontal shore platform, Tatapouri, North Island, New Zealand. *Continental Shelf Research* **31**, 1409–1419 (2011).

74. S. T. Hallowell, S. R. Arwade, C. Qiao, A. T. Myers, W. Pang, Breaking Wave Hazard Estimation Model for the U.S. Atlantic Coast. *ASCE-ASME Journal of Risk and Uncertainty in Engineering Systems, Part B: Mechanical Engineering* **7**, 040904 (2021).

75. C. E. Stringari, H. E. Power, The Fraction of Broken Waves in Natural Surf Zones. *JGR Oceans* **124**, 9114–9140 (2019).

76. M. C. Sarofim, *et al.*, High radiative forcing climate scenario relevance analyzed with a ten-million-member ensemble. *Nat Commun* **15**, 8185 (2024).

77. N. Scafetta, Impacts and risks of “realistic” global warming projections for the 21st century. *Geoscience Frontiers* **15**, 101774 (2024).

78. E. Kirezci, *et al.*, Projections of global-scale extreme sea levels and resulting episodic coastal flooding over the 21st Century. *Sci Rep* **10**, 11629 (2020).

79. J. Hinkel, *et al.*, Coastal flood damage and adaptation costs under 21st century sea-level rise. *Proc. Natl. Acad. Sci. U.S.A.* **111**, 3292–3297 (2014).

80. J.-P. Avouac, From Geodetic Imaging of Seismic and Aseismic Fault Slip to Dynamic Modeling of the Seismic Cycle. *Annu. Rev. Earth Planet. Sci.* **43**, 233–271 (2015).

81. R. Govers, K. P. Furlong, L. Van De Wiel, M. W. Herman, T. Broerse, The Geodetic Signature of the Earthquake Cycle at Subduction Zones: Model Constraints on the Deep Processes. *Reviews of Geophysics* **56**, 6–49 (2018).

82. H. Perfettini, J. -P. Avouac, J. -C. Ruegg, Geodetic displacements and aftershocks following the 2001 M_w = 8.4 Peru earthquake: Implications for the mechanics of the earthquake cycle along subduction zones. *J. Geophys. Res.* **110**, 2004JB003522 (2005).

83. J. Sauber, G. Carver, S. Cohen, R. King, Crustal deformation and the seismic cycle across the Kodiak Islands, Alaska. *J. Geophys. Res.* **111**, 2005JB003626 (2006).

84. K. Wang, Y. Hu, J. He, Deformation cycles of subduction earthquakes in a viscoelastic Earth. *Nature* **484**, 327–332 (2012).

85. B. P. Horton, *et al.*, Microfossil measures of rapid sea-level rise: Timing of response of two microfossil groups to a sudden tidal-flooding experiment in Cascadia. *Geology* **45**, 535–538 (2017).

86. L. J. Leonard, C. A. Currie, S. Mazzotti, R. D. Hyndman, Rupture area and displacement of past Cascadia great earthquakes from coastal coseismic subsidence. *Geological Society of America Bulletin* **122**, 2079–2096 (2010).

87. B. P. Horton, *et al.*, Microfossil measures of rapid sea-level rise: Timing of response of two microfossil groups to a sudden tidal-flooding experiment in Cascadia. *Geology* **45**, 535–538 (2017).

88. A. J. Meltzner, *et al.*, Coral evidence for earthquake recurrence and an A.D. 1390–1455 cluster at the south end of the 2004 Aceh–Andaman rupture. *J. Geophys. Res.* **115**, 2010JB007499 (2010).

89. J. Wahr, M. Wyss, Interpretation of postseismic deformation with a viscoelastic relaxation model. *J. Geophys. Res.* **85**, 6471–6477 (1980).

90. C. Martínez, D. Rojas, M. Quezada, J. Quezada, R. Oliva, Post-earthquake coastal evolution and recovery of an embayed beach in central-southern Chile. *Geomorphology* **250**, 321–333 (2015).

91. H. Luo, K. Wang, Finding Simplicity in the Complexity of Postseismic Coastal Uplift and Subsidence Following Great Subduction Earthquakes. *JGR Solid Earth* **127** (2022).

92. H. Suito, J. T. Freymueller, A viscoelastic and afterslip postseismic deformation model for the 1964 Alaska earthquake. *J. Geophys. Res.* **114**, 2008JB005954 (2009).

93. K. Berryman, K. Clark, U. Cochran, A. Beu, S. Irwin, A geomorphic and tectonic model for the formation of the flight of Holocene marine terraces at Mahia Peninsula, New Zealand. *Geomorphology* **307**, 77–92 (2018).

94. H. Matsumoto, M. E. Dickson, P. S. Kench, Preservation and Destruction of Holocene Marine Terraces: The Effects of Episodic Versus Gradual Relative Sea Level Change. *Geophysical Research Letters* **48**, e2021GL094543 (2021).

95. M. Saillard, *et al.*, From the seismic cycle to long-term deformation: linking seismic coupling and Quaternary coastal geomorphology along the Andean megathrust: Interseismic Coupling/Coastal Morphology. *Tectonics* **36**, 241–256 (2017).

96. L. C. Malatesta, L. Bruhat, N. J. Finnegan, J. L. Olive, Co-location of the Downdip End of Seismic Coupling and the Continental Shelf Break. *JGR Solid Earth* **126** (2021).

97. H. M. Kelsey, J. G. Bockheim, Coastal landscape evolution as a function of eustasy and surface uplift rate, Cascadia margin, southern Oregon. *Geological Society of America Bulletin* **106**, 840–854 (1994).

98. R. S. Anderson, K. M. Menking, The Quaternary marine terraces of Santa Cruz, California: Evidence for coseismic uplift on two faults. *Geol Soc America Bull* **106**, 649 (1994).

99. R. S. Anderson, Evolution of the Northern Santa Cruz Mountains by Advection of Crust Past a San Andreas Fault Bend. *Science* **249**, 397–401 (1990).

100. S. L. Horton, M. E. Dickson, W. J. Stephenson, The consequences of uplift on wave transformation across a shore platform, Kaikōura, New Zealand. *Marine Geology* **451**, 106888 (2022).

101. P. N. Adams, C. D. Storlazzi, R. S. Anderson, Nearshore wave-induced cyclical flexing of sea cliffs. *J. Geophys. Res.* **110**, 2004JF000217 (2005).

102. P. Letortu, S. Costa, J. Cador, C. Coinaud, O. Cantat, Statistical and empirical analyses of the triggers of coastal chalk cliff failure. *Earth Surf Processes Landf* **40**, 1371–1386 (2015).

103. N. J. Rosser, M. J. Brain, D. N. Petley, M. Lim, E. C. Norman, Coastline retreat via progressive failure of rocky coastal cliffs. *Geology* **41**, 939–942 (2013).

104. C. J. Hapke, D. Reid, "National Assessment of Shoreline Change Part 4: Historical Coastal Cliff Retreat along the California Coast" (USGS, 2007).

105. G. R. Priest, Coastal Shoreline Change Study Northern and Central Lincoln County, Oregon. *Journal of Coastal Research* 140–157 (1999).

106. P. Ruggiero, *et al.*, "National assessment of shoreline change: historical shoreline change along the Pacific Northwest coast" (USGS, 2013).

107. B. Leshchinsky, *et al.*, Mitigating coastal landslide damage. *Science* **357**, 981–982 (2017).

108. R. Castedo, C. Paredes, R. D. L. Vega-Panizo, A. P. Santos, "The Modelling of Coastal Cliffs and Future Trends" in *Hydro-Geomorphology - Models and Trends*, D. P. Shukla, Ed. (InTech, 2017).

109. M. B. Bryant, *et al.*, Multiple modes of shoreline change along the Alaskan Beaufort Sea observed using ICESat-2 altimetry and satellite imagery. *The Cryosphere* **19**, 1825–1847 (2025).

110. P. N. Adams, R. S. Anderson, J. Revenaugh, Microseismic measurement of wave-energy delivery to a rocky coast. *Geol* **30**, 895 (2002).

111. C. S. Earlie, A. P. Young, G. Masselink, P. E. Russell, Coastal cliff ground motions and response to extreme storm waves. *Geophysical Research Letters* **42**, 847–854 (2015).

112. Z. M. Swirad, A. P. Young, Hazard of coastal cliff top failure through time. *Geomorphology* **481**, 109791 (2025).

113. A. P. Young, P. N. Adams, W. C. O'Reilly, R. E. Flick, R. T. Guza, Coastal cliff ground motions from local ocean swell and infragravity waves in southern California. *J. Geophys. Res.* **116**, C09007 (2011).

114. A. P. Young, R. T. Guza, M. E. Dickson, W. C. O'Reilly, R. E. Flick, Ground motions on rocky, cliffed, and sandy shorelines generated by ocean waves. *JGR Oceans* **118**, 6590–6602 (2013).

115. S. Saramul, T. Ezer, Spatial variations of sea level along the coast of Thailand: Impacts of extreme land subsidence, earthquakes and the seasonal monsoon. *Global and Planetary Change* **122**, 70–81 (2014).

116. K. Udo, D. Sugawara, H. Tanaka, K. Imai, A. Mano, Impact of the 2011 Tohoku Earthquake and Tsunami on Beach Morphology Along the Northern Sendai Coast. *Coastal Engineering Journal* **54**, 1250009-1-1250009–15 (2012).

117. B. J. Yanites, *et al.*, Cascading land surface hazards as a nexus in the Earth system. *Science* **388**, eadp9559 (2025).

118. D. E. Hart, S. J. Pitman, D.-S. Byun, Earthquakes, Coasts… and Climate Change? Multi-hazard Opportunities, Challenges and Approaches for Coastal Cities. *Journal of Coastal Research* **95**, 819 (2020).